Since January 2020 Elsevier has created a COVID-19 resource centre with free information in English and Mandarin on the novel coronavirus COVID-19. The COVID-19 resource centre is hosted on Elsevier Connect, the company's public news and information website.

Biomedical Signal Processing and Control 69 (2021) 102800

Contents lists available at ScienceDirect

Biomedical Signal Processing and Control

journal homepage: www.elsevier.com/locate/bspc

A morphology-based radiological image segmentation approach for efficient screening of COVID-19

Shouvik Chakraborty *, Kalyani Mali

Department of Computer Science and Engineering, University of Kalyani, India

ARTICLE INFO

Keywords:
COVID-19
Unsupervised clustering
Morphology
Computer vision
Pattern matching

ABSTRACT

Computer-aided radiological image interpretation systems can be helpful to reshape the overall workflow of the COVID-19 diagnosis process. This article describes an unsupervised CT scan image segmentation approach. This approach begins by performing a morphological reconstruction operation that is useful to remove the effect of the external disturbances on the infected regions and to locate different regions of interest precisely. The optimal size of the structuring element is selected using the Edge Content-based contrast matrix approach. After performing the opening by using the morphological reconstruction operation, further noise is eliminated using the closing-based morphological reconstruction operation. The original pixel space is restored and the obtained image is divided into some non-overlapping smaller blocks and the mean intensity value for each block is computed that is used as the local threshold value for the binarization purpose. It is preferable to manually determine the range of the infected region. If a region is greater than the upper bound then that region will be considered as an exceptional region and processed separately. Three standard metrics MSE, PSNR, and SSIM are used to quantify the outcomes. Both quantitative and qualitative comparisons prove the efficiency and real-life adaptability of this approach. The proposed approach is evaluated with the help of 400 different images and on average, the proposed approach achieves MSE 307.1888625, PSNR 23.7246505, and SSIM 0.831718459. Moreover, the comparative study shows that the proposed approach outperforms some of the standard methods and obtained results are encouraging to support the battle against the COVID-19.

1. Introduction

The whole world is currently facing a major threat due to the recent outbreak of the 2019 novel coronavirus disease or COVID-19 virus and many countries currently going through a pandemic scenario. 141,057,106 total confirmed cases are reported to the world health organization (WHO) among which 3,015,043 people expired around the world due to this disease till 4:28 pm CEST, 19th April 2021 [1]. From these statistics, it is clear that the approximate mortality rate is 2.137 % throughout the world but, the mortality rate is merely a statistical figure but does not show a clear picture of the present scenario because the rate of infection is growing exponentially and much higher compared to the number of casualties. The highly infectious nature of the COVID-19 virus leads to a pathetic condition throughout the world and many countries are not in a state to provide sufficient infrastructures that are required to support the infected patients as well as healthy patients from getting infected. The recently observed mutations make the situation worse. Specifically, some dedicated drugs are required to effectively fight against this highly infectious virus. At present, some precautionary measures like social distancing, isolation, use of masks, sanitizers, hand wash, face shield, and other protective gear, etc. are considered as some of the important and effective tools to prevent the drastic spread of this disease. People from many remote geographic locations are also not able to maintain all prescribed precautionary measures due to not having sufficient resources or a lack of relevant knowledge.

The reverse transcription-polymerase chain reaction (RT-PCR) test is frequently used and the gold standard to detect and confirm the presence of the COVID-19 virus. Some studies show that radiological images can be helpful in the diagnosis process [2–10]. Chest CT scan images are useful in this context because some prominent features can be observed in these images which can be considered as the early signs of the COVID-19 infection [11]. It is an important observation because CT scan images of the chest region can be useful to detect and analyze the suspected patients quickly so that, the isolation process can get accelerated and the drastic spread of this virus can be decelerated to some extent. Moreover, radiological investigations can be performed with minimal

* Corresponding author.
E-mail addresses: shouvikchakraborty51@gmail.com (S. Chakraborty), kalyanimali1992@gmail.com (K. Mali).

https://doi.org/10.1016/j.bspc.2021.102800
Received 17 January 2021; Received in revised form 9 May 2021; Accepted 15 May 2021
Available online 19 May 2021

contact with the patients which is essential to keep the technicians and other medical professionals safe from this infection. CT scan images can be considered a useful tool for the screening purpose [12] but should not be used as an alternative to the RT-PCR test because some false positive cases are reported in [13,14]. Moreover, sometimes false negative reports may also get generated due to the status of infection in the chest region. But some prominent features are quite encouraging and effective to investigate the CT scan images for early screening purposes. Image segmentation is important and sometimes very useful from the context of automated biomedical image analysis frameworks [15–17]. Automated and intelligent computer-aided diagnostic systems are highly beneficial to automate the manual diagnostic procedures and helpful for the physicians to avoid typical man-made errors. The proposed work can aid the diagnosing process of COVID-19 pneumonia from some prominent symptoms, not the infection itself, that can only be confirmed with the help of some standard procedures like the RT-PCR test. It should also be noted that the proposed approach cannot replace the role of the gold-standard test RT-PCR in the diagnostic process.

Time is an important resource for automated diagnostic systems because delay in the diagnosis process results in a delay in the treatment and there sore, time is highly important to save many precious lives. Automated diagnostic systems can work in a highly time-bound manner and can act as a helping hand of the physicians. Image segmentation is an inextricable component for most of the automated image exposition frameworks [18–20]. It prepares an image in such a way so that, the image is easy to interpret and the root cause of a disease can be easily understood [19,21].

Computer vision and machine learning are the allied domains of artificial intelligence which are frequently used to solve various practical problems because these approaches can uncover some hidden patterns and information from the underlying dataset which are may not be always feasible by human observers. The ability to scale CT is much harder than lab tests but the RT-PCR test is time-consuming (the turnaround time is approximately 10−15 h after receiving the sample from the suspected patient). Moreover, this work is not intended to replace these conventional tests by any means and intended to support the physicians so that they can effectively interpret the radiological images.

Machine learning approaches can be categorized into two broad ways like unsupervised and supervised approaches [21–26]. Supervised approaches require some training data from where they can learn or understand the dataset and act accordingly. Unsupervised approaches explore the dataset under consideration without being guided or trained by any training samples [27,28]. In general, expert delineations of the CT scan images which are collected from the COVID-19 positive patients are not always available. Therefore, in this work, a novel segmentation approach is proposed for the CT scan images which can be proved as an efficient tool to combat the spread of the COVID-19 virus [10,29]. Although, CT scans will likely have little effect to combat the spread as the patient is already in the hospital, not the community but, early diagnosis can refrain doctors, nurses, hospital staffs, and other patients in the hospital from getting infected. Moreover, it is not the case that patients with some minor problems always get themselves admitted to the hospital. From that point of view, the proposed work can help to combat the spread of this virus to some extent.

The proposed approach addresses the challenging task to automate the segmentation process of the CT scan images which are collected from the chest region of the COVID-19 infected patients. The proposed approach is based on morphological operations. All images that are used in this work are collected from public repositories and it is ensured that there is no requirement of taking any kind of consent from any person organization the privacy of the patients is not violated at all. The input image is first processed with the morphological reconstruction operation which is supported by the Edge Content-based contrast matrix approach to finding the optimal size of the structuring element. The input image is then segmented using some morphological operations and by approximating the elliptic shape of the alveoli. The proposed approach is described in Section 3 in detail. The proposed approach is tested on some of the standard real-life CT scan images which are collected from the chest region of the COVID-19 infected patients. Moreover, the proposed approach is compared with four existing approaches using both quantitative and qualitative manners. The obtained results are discussed in detail in Section 4.

The remaining article is organized as follows: Section 2 describes some of the related works in brief. Sections 3 and 4 discuss the proposed approach and the corresponding results in detail respectively. Section 5 concludes the article by discussing some important and relevant points and also by giving some future directions.

2. Related works

In this section, some related works which are related to the COVID-19 image data analysis are discussed in brief. The overall literature can be broadly divided into two parts e.g., works that are based on X-ray images and works based on CT images. Among the following discussed literature, the first five works are based on the X-ray images whereas the next five works are based on the CT images. These works are mostly supervised. The last paragraph is dedicated to discussing some of the closely related works.

A deep learning model based COVID-19 image classification framework is proposed in [30]. This work uses X-ray images to identify COVID-19 infection. This approach is named COVIDX-net and it integrates seven different deep neural network architectures. This work is tested using a small amount of image data and shows a satisfactory performance. This approach achieves a 0.89 F1 score for normal samples and a 0.91 F1 score for COVID-19 infected samples. Another deep learning-based COVID-19 image analysis framework is proposed in [31] and this work also uses the X-ray images for the classification purpose. This model is named COVID-Net and it is applied on a large number of X-ray images and shows some promising results. The authors explain the working principle of this classification architecture in detail. Moreover, an unbiased audit of this deep learning model is presented to validate the classification results. This approach achieves 93.3 % accuracy, 91.0 % sensitivity, and 98.9 % PPV in analyzing COVID-19 images. A similar approach i.e. deep learning-based X-ray image classification method is proposed in [32] which is named DarkCovidNet. In this work, a heat map-based infected region detection mechanism is proposed. This model is used in both binary and multi-class classification problems and achieved 98.08 % and 87.02 % accuracy from these two types of problems respectively. Another X-ray based automated image classification framework is proposed in [33] to automate the diagnosis process of the COVID-19 disease. This work is based on the deep Bayes-SqueezeNet network and named COVIDiagnosis-Net. The proposed approach outperforms some of the existing approaches in terms of performance once the hyper-parameters are fine-tuned. This approach achieves 98.3 %

accuracy, correctness, F1 score, and completeness; 99.1 % Specificity, and 97.4 % Matthew Correlation Coefficient values. A convolutional neural network based automated COVID-19 image analysis architecture is proposed in [34]. This approach is based on the X-ray images and two datasets are involved with three different types of the images such as confirmed COVID-19 positive cases, bacterial and viral pneumonia, and normal cases. The proposed approach can find some interesting and useful patterns from these images with 96.78 % accuracy, 98.66 % sensitivity, and 96.46 % specificity.

Multivariate logistic regression-based COVID-19 radiological image diagnosis models are proposed in [35]. In this work, three models are proposed which are quantitatively evaluated using the receiver operating characteristic curve. Both semantic and clinical properties are considered in this work. A total of 18 semantic and 17 clinical features are considered and these properties are significantly different and some well-known statistical tests are used to establish this fact. The proposed models prove to be efficient compared to some of the existing works. This approach achieves a 98.6 % area under curve (AUC) value. A deep learning framework-based COVID-19 CT scan image analysis approach is proposed in [36]. In this work, both two-dimensional and three-dimensional deep learning models are adapted and these models along with some variations are applied and tested on various international datasets. The experiments show some encouraging results with a 0.996 area under the curve. This approach can be helpful in the detection as well as monitoring of the COVID-19 infected patients. A CT scan image analysis framework based on deep learning is proposed in [37]. In this work, a commercially available deep learning architecture is used to quantify and assess CT scan images. Patients are categorized into different classes depending on the severity of the infection. A total of 126 patients are considered for the experiments and it is observed that this approach can remove the subjective dependency from the test images and helps to efficiently quantify these images. With the help of this approach, a 3.6 % increase in the opacification is observed in baseline CT to first follow-up CT image. But it is interesting to note that the opacification does not increase significantly from the first to the second follow-up CT image. An automated deep learning-based CT scan image analysis framework is developed in [28]. A total 5372 number of patients are considered to collect the samples of the CT scan. The system is trained with 4106 images and then 1266 images are used to test the performance of the system. Moreover, four external validation sets are used and the performance of this classifier is quite impressive in identifying COVID-19 patients from other classes. This approach can effectively identify COVID-19 pneumonia from other pneumonia, and viral pneumonia with the area under curve 0.87, 0.88, and 0.86 respectively. A multi-objective approach coupled with a convolutional neural network-based approach for COVID-19 is proposed in [38]. This work can classify into two classes i.e., infected and non-infected. The hyperparameters of the convolutional neural network are fine-tuned using the multi-objective differential evolution algorithm. The experiments prove the efficiency of this approach. This approach outperforms some other state-of-the-art models, i.e., ANN, ANFIS, and CNN models in terms of accuracy, F-measure, sensitivity, specificity, and Kappa statistics by 1.9789 %, 2.0928 %, 1.8262 %, 1.6827 %, and 1.9276 %, respectively.

An approach for COVID-19 infected chest CT image segmentation is proposed in [39]. This approach is dependent on the voxel-level anomaly modeling that can effectively find some of the important and relevant information about the healthy CT image. This work does not depend on any labeled or annotated data. The training pairs are generated by including synthetic lesions. These training pairs are used to learn normalcy-recognizing networks or NormNet. This work is validated with the help of three publicly available datasets namely Coronacases, Radiopedia, and UESTC and it is observed that it outperforms many state-of-the-art unsupervised anomaly detection techniques and achieves AUC value 87.0, 89.7, and 88.4 respectively. A weakly-supervised approach for COVID-19 chest CT image segmentation purposes is proposed in [40]. This approach is designed to help the physicians in rapid detection of the presence of this infection with a limited number of labeled datasets. This approach implements a pipeline of methods that deals with different jobs like segmentation of the lung region, classification of the two-dimensional slice, and localization, etc. This approach proposes an unsupervised clustering that exploits the feature space. This approach is tested on an external dataset with images collected from 199 patients and the results are found to be satisfactory enough. It achieves 100 % accuracy, and specificity, precision, F1-score, and sensitivity on volume level evaluation. Another semi-supervised approach is proposed in [41] that uses limited amount of samples for the detection purposes. This approach proposes a regularized semi-supervised framework that is based on an active contour model. The region-scalable fitting model is used to realize the active contour-based approach. It is observed that this approach outperforms many state-of-the-art techniques in terms of different well-known metrics up to 5% in dice similarity, 8 mm in 95 % Hausdorff distance, and 10 % in relative absolute volume difference. An unsupervised approach is proposed in [29] for the early understanding of the COVID-19 infection from the radiological images. This approach exploits the advantages of superpixels to reduce the computational overhead that is associated with the processing of a significantly large amount of spatial information. This approach hybridizes the type-2 fuzzy system and modified flower pollination optimization approach to determine the optimal clustering outcome. This approach is free from the selection of the initial cluster centers. Experimental results prove the superiority of this approach over many existing approaches. On average, this approach achieves Davies-Bouldin index value 1.320236, 1.639451, 1.744748, 1.522415 for 3, 5, 7, and 9 clusters respectively. An unsupervised approach for COVID-19 infected lung CT image segmentation is proposed in [42] that is based on representational learning and clustering. This approach proposes a pre-processing algorithm to avoid segmenting high-intensity regions as infected ones. This approach proves to be efficient and shows a significant improvement in mutual information score and achieves 0.394 e normalized mutual information score.

Apart from these approaches, some comprehensive reviews on the same topic can be found in [6,43–46] that can be beneficial in further research.

3. Proposed approach

In this section, the proposed morphology-based CT image segmentation approach is discussed in detail. The proposed approach is demonstrated in algorithm 1.

Algorithm 1: The proposed morphology-based CT image segmentation approach

Input: A CT image

Output: The corresponding segmented CT scan image

1. Complement the actual image using equation 1.
2. Perform morphological opening based reconstruction operation using equation 2.
3. Use the Edge Content-based contrast matrix approach to determine the optimal size of the structuring element.
4. Apply equation 6 to reduce further noise using morphological closing-based reconstruction operation.
5. Get back the actual pixel space using equation 8.
6. Divide the obtained image into some non-overlapping smaller blocks.
7. Find the value of the mean intensity for each block.
8. Binarize the image using equation 9 by considering the mean values of each block as the local threshold values.
9. Determine the 8 connected components from the obtained binary image to initially highlight the possible infected regions.
10. Determine the range $[Ar_{lb}, Ar_{ub}]$ of the infected region. (Manual investigation is preferred)
11. Check if $Area(R_k) > Ar_{ub}$ then
    a. Consider the region R_k as an exceptional region and find the range $[d_{lb}, d_{ub}]$ by computing the minimum and the maximum gray-level intensity values of that region.
    b. Find the threshold value th_e using equation 10
    c. Repeat for all $th_e \in [d_{lb}, d_{ub}]$
        i. Apply equation 11 to binarize an exceptional region.
        ii. Find the τ number of disconnected regions $\{M_t\}_{t=1,2,3,.....,\tau}$.
        iii. Find penalty which is introduced due to the ellipticity property using equation 12.
        iv. Find the penalty for the area of a region M_t using equation 13.
        v. Determine the value of the cost function.
    end repeat
    d. Determine the optimal threshold value using equation 15.
    end if
12. Apply morphological opening to further smooth the obtained image.
13. Return the final segmented outcome

The proposed approach begins by performing a morphological reconstruction operation. This step is useful to remove the effect of the external disturbances on the infected regions and to locate different regions of interests precisely. The reconstruction process starts by complementing the actual image I using Eq. (1). The maximum possible gray-level intensity value is denoted by $I_{\max}$.

$$I^c = I_{\max} - I(p,q) \tag{1}$$

The obtained complemented image i.e. I^c is used to take part in the morphological opening based reconstruction operation [47] and it is defined in Eq. (2).

$$\widehat{I} = \Re\left(I^c_{erosion}, I^c\right) \tag{2}$$

The morphological opening based reconstruction operation is denoted by $\Re$. $I^c_{erosion}$ is mathematically expressed using Eq. (3).

$$I^c_{erosion} = I^c \circ E_s \tag{3}$$

In this equation, $\circ$ denotes the erosion operation and E_s is the structuring element. The structuring element plays a crucial role and the selection of the structuring element is a challenging task for different types of images and features. It is essential to determine the size of the structuring element automatically to generate better quality results. Moreover, rotation invariance is also a required attribute for the selection of the structuring elements. In this work, the disk structuring element is considered because it is rotation invariant. The optimal size of the structuring element is selected using the Edge Content-based contrast matrix approach [48]. The disk structuring element is typically controlled by the size of the radius *rad*. The edge content value is used as the prime tool to determine the best size of the radius. To determine the optimal value of the radius, the edge content value is rigorously searched for the radius range $3 \leq rad \leq 65$. This approach works because, the value of the edge content is increased proportionally with the size of the radius up to some extent and these two parameters are directly proportional i.e., the value of the edge content will increase with the increasing value of the radius up to some extent and after a certain threshold, increase in the radius value will not affect the value of the edge content in a significant manner. The search can be stopped when some successive iterations do not significantly change the value of the edge content. The value of the edge content is calculated using the magnitude of the gradient vector. The gradient vector of an image I at a certain position (p,q) can be computed using Eq. (4) and the

Table 1
Description of the fourteen test images whose results are presented in this article.

Image Id	View	Source	Gender	Age	Observed properties	Comments/Remarks
I^{01}	Coroanal	[54]	Female	50	ground-glass opacities (GGO)	Case courtesy of Dr Bahman Rasuli, Radiopaedia.org, rID: 75329
I^{02}	Axial					
I^{03}	Axial	[55]	Male	75	ground-glass opacities (GGO) crazy paving enlarged mediastinal lymph nodes	Case courtesy of Dr Fabio Macori, Radiopaedia.org, rID: 74867
I^{04}	Coronal					
I^{05}	Axial				ground-glass opacities (GGO)	
I^{06}	Coronal	[56]	Female	70	crazy paving	Case courtesy of Dr Ammar Haouimi, Radiopaedia.org, rID: 75665
I^{07}	Sagittal				air space consolidation	
I^{08}	Sagittal					
I^{09}	Axial	[57]	Male	50	ground-glass opacities (GGO)	Case courtesy of Dr Ammar Haouimi, Radiopaedia.org, rID: 76295
I^{10}	Coronal					
I^{11}	Frontal	[58]	Male	25	Normal	Case courtesy of Dr Andrew Dixon, Radiopaedia.org, rID: 36676
I^{12}	Axial	[59]	Male	55	Usual interstitial pneumonia (UIP)	Case courtesy of Dr Hani Makky Al Salam, Radiopaedia.org, rID: 13199
I^{13}	Axial	[60]	Female	35	Normal	Case courtesy of Dr Bruno Di Muzio, Radiopaedia.org, rID: 41162
I^{14}	Coronal	[61]	Female	35	Pulmonary mucormycosis	Case courtesy of Dr David Holcdorf, Radiopaedia.org, rID: 64718

corresponding edge content value can be computed using Eq. (5).

$$\nabla I(p,q) = \begin{bmatrix} Grad_p \\ Grad_q \end{bmatrix} = \begin{bmatrix} \frac{\partial}{\partial p} I(p,q) \\ \frac{\partial}{\partial q} I(p,q) \end{bmatrix} \tag{4}$$

$$edge\ Content = \frac{1}{u \times v} \sum_{p} \sum_{q} |\nabla I(p,q)| \tag{5}$$

The effect of the value of the radius on the value edge content is numerically illustrated in the next section.

After performing the opening by using the morphological reconstruction operation, further noise can be eliminated using the closing based morphological reconstruction operation and it is defined in Eq. (6).

$$\widehat{I} = I_{\max} - \Re\left(\widehat{I}^{'} \circ E_s, \widehat{I}^{'}\right) \tag{6}$$

In this equation, $\widehat{I}^{'}$ can be mathematically expressed by Eq. (7).

$$\widehat{I}^{'} = I_{\max} - \widehat{I} \tag{7}$$

After this step, $\widehat{I}$ needs to be mapped back to the actual pixel space and it can be performed using Eq. (8).

$$I^{'}(p,q) = I_{\max} - \widehat{I}^{'}(p,q) \tag{8}$$

To segment the image $I^{'}$, adaptive thresholding-based approach is used in the very first stage. This process begins by dividing the image $I^{'}$ in to small blocks. The division process is carried out in such a way so that no overlapping is there among the blocks. The value of the mean intensity of every block is computed. This value is considered as the value of the local threshold th_l. Eq. (9) is used to binarize the image based on the local threshold values.

$$I^{bin}(p,q) = \begin{cases} 0 & if\ I^{'}(p,q) \le th_l \\ 1 & otherwise \end{cases} \tag{9}$$

The above equation works under the assumption that the infected regions of the chest CT scans appear brighter compared to its surroundings. Eight-connected components are determined from the binary image I^{bin}. It is helpful to initially mark the probably infected regions $\{R_i\}_{i=1,2,3,\ldots,x}$ of the image where, x is the number of regions. Variations in the local gray-level intensity values can cause a significant problem in detecting the infected regions due to some under segmented regions. To solve this problem, some domain associated information must take into consideration. Typically, the size and shape of the infected regions can vary depending on the different types of cases. The overall area of the infected region is within the range $[Ar_{lb}, Ar_{ub}]$ where Ar_{lb} and Ar_{ub} are the lower and the upper bound of the infected area respectively. These values can be decided manually by investigating different cases or automatically depending on the observed fitness values. If the area of the k^{th} region R_k is more than the upper bound i.e. $Area(R_k) > Ar_{ub}$ then that region can be safely considered as an exception. For these cases, the upper and the lower intensity values are computed to estimate the dynamic range of these regions, which is helpful to re-segment these regions in smaller regions. The dynamic range can be expressed as $[d_{lb}, d_{ub}]$ where d_{lb} and d_{ub} are the lower and the upper value of the gray-level intensity in an exceptional region. This range is used to determine a threshold value th_e is computed using Eq. (10).

$$th_e = d_{ub} - itrCnt - 1 \tag{10}$$

In this equation, *itrCnt* denotes the count of iteration. This threshold value is used to segment the exceptional regions into subregions using Eq. (11).

$$P^{bin}(p,q) = \begin{cases} 0 & if\ P(p,q) \le th_e \\ 1 & otherwise \end{cases} \tag{11}$$

In this equation, $P(p,q)$ represents the value of the gray-level intensity of a pixel. If the image P^{bin} consists of τ number of disconnected regions $\{M_t\}_{t=1,2,3,\ldots,\tau}$. Typically, some signs of the infection can be visible in the alveoli of the lungs and alveoli are generally formed as a grape object. So, without losing the generality, it can be thought that the signs of the infection can be detected from the pattern of the alveoli because lungs is constructed with many of them [49,50]. Alveoli are of grape shaped so, it can be approximated by fitting an ellipse [51,52]. Now, for a certain disconnected region M_t, the penalty which is introduced due to the ellipticity property can be computed using Eq. (12).

$$\Upsilon_e(M_t) = \frac{|\alpha(M_t) \perp \beta(M_t)|}{|\beta(M_t)|} \tag{12}$$

In this equation, Υ_e denotes the penalty parameter, $\alpha(M_t)$ denotes the collection of points in the region M_t and $\beta(M_t)$ represents the collection of points that belongs to the best fitted ellipse. $\perp$ is an operator that computes the symmetric difference between two sets and $|\cdot|$ denotes the cardinality of a set. The direct least square fitting approach [53] is adapted in this work to fit an ellipse in a region M_t. It is worth mentioning here that if an ellipse perfectly fits the region M_t then

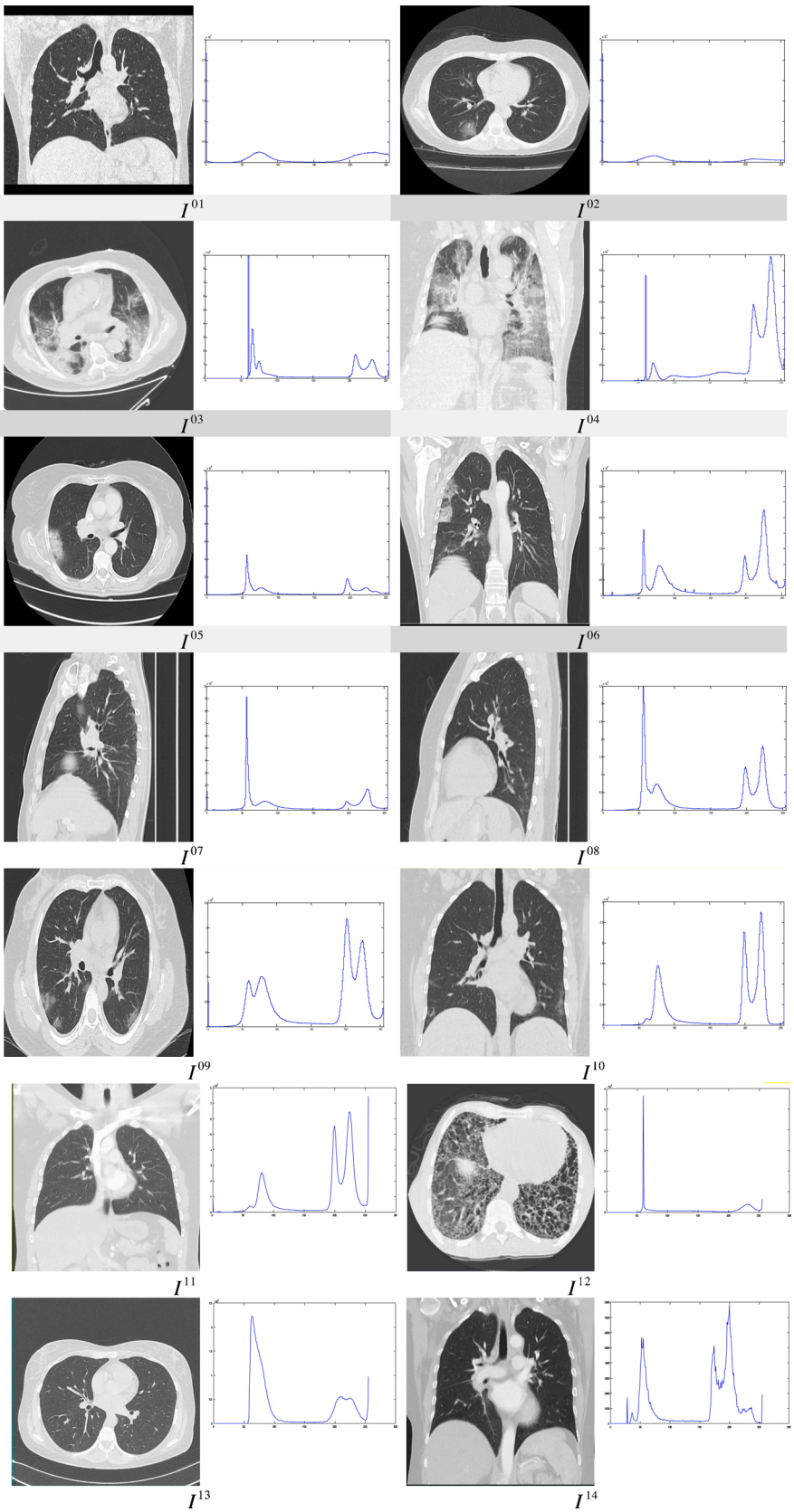

Fig. 1. Fourteen test images along with their corresponding histograms.

Table 2
Value of the edge content with the value of the radius.

Image Id	Value of the radius										
	3	9	14	20	25	31	36	42	50	56	65
I^{01}	0.0625	0.07968	0.099362	0.106036	0.10936	0.110236	0.11056325	0.1137089	0.1159063	0.117086	0.119063
I^{02}	0.062882687	0.081804802	0.106263924	0.106962947	0.112160614	0.112408988	0.119024621	0.120374806	0.12079255	0.121741921	0.12382448
I^{03}	0.065709478	0.083181756	0.107450189	0.107813428	0.111960727	0.115269455	0.116474817	0.118002548	0.121326404	0.122377748	0.124243293
I^{04}	0.065380133	0.089370226	0.099807493	0.111265811	0.111722479	0.112844892	0.115045962	0.116163096	0.119433011	0.122865489	0.126936882
I^{05}	0.068385926	0.084914459	0.108696937	0.110073288	0.112120828	0.112760574	0.115683904	0.118033998	0.118557853	0.119243809	0.11989543
I^{06}	0.068344824	0.085011965	0.103016637	0.106514226	0.111031533	0.112839955	0.116348032	0.117926906	0.118053798	0.118459772	0.12857676
I^{07}	0.062816786	0.087001089	0.107534541	0.113716998	0.115585757	0.117980078	0.118511111	0.119058046	0.120227777	0.120392798	0.121522283
I^{08}	0.071031104	0.08921321	0.105608835	0.108106657	0.110578	0.112349308	0.113733924	0.117432822	0.117913927	0.123913343	0.127508529
I^{09}	0.068236938	0.08702662	0.109235972	0.109713136	0.112319407	0.114271686	0.11740463	0.117636613	0.117784754	0.118139749	0.127298523
I^{10}	0.066613194	0.08833263	0.103937137	0.112187834	0.115456562	0.115948786	0.118229546	0.119173935	0.119228231	0.120728367	0.125747827
I^{11}	0.053762558	0.063542164	0.096510756	0.103476709	0.1057197429	0.09035473	0.1111420232	0.107799937	0.117722726	0.130186346	0.132862416
I^{12}	0.066581637	0.069783306	0.080556957	0.104926567	0.127805516	0.133912074	0.122757147	0.110444219	0.123091017	0.129196597	0.13766194
I^{13}	0.072861	0.071233	0.093143	0.11662	0.115251	0.11612	0.122513	0.123568	0.122255	0.124857	0.138323
I^{14}	0.068651755	0.07269373	0.092884143	0.11965492	0.119093062	0.114012229	0.117035963	0.127691002	0.121347053	0.122630976	0.137542701

$\Upsilon_e(M_t) = 0$. The penalty for the area of a region M_t can be computed using Eq. (13).

$$\Upsilon_a(M_t) = \begin{cases} 0 & if\ Ar_{lb} \le Area(M_t) \le Ar_{ub} \\ \dfrac{Ar_{lb} - Area(M_t)}{\frac{1}{2}(Ar_{lb} + Ar_{ub})} & if\ 0 < Area(M_t) < Ar_{lb} \\ \dfrac{Area(M_t) - Ar_{ub}}{\frac{1}{2}(Ar_{lb} + Ar_{ub})} & if\ Area(M_t) > Ar_{ub} \end{cases} \tag{13}$$

In this equation, $Area(M_t)$ find the area of a region M_t. Two penalty terms Υ_e and Υ_a helps to incorporate the domain knowledge to the segmentation process. A cost function is designed in Eq. (14) based on these two penalty terms and the threshold value th_e.

$$\Psi(th_e) = \frac{1}{\tau}\sum_{x=1}^{\tau}[\Upsilon_e(M_t) + \Upsilon_a(M_t)] \tag{14}$$

Here, τ denotes the number of disconnected regions. This cost function gives the overall penalty of the τ number of disconnected regions. It can be clearly understood that if the area of the segmented region belongs to the range $[Ar_{lb}, Ar_{ub}]$ and it close to the elliptical shape then the value of the cost function will be smaller.

The optimal threshold is obtained iteratively where the iterations are continued for all possible thresholds $th_e \in [d_{lb}, d_{ub}]$. Eq. (15) can be used to determine the optimal threshold value.

$$th_{optimal} = \arg_{th}\min[\Psi(th_e)] \tag{15}$$

In the final phase, the segmented image is further smoothed using the morphological opening.

4. Results of the simulation

The main objective of this approach is to effectively identify the infected region from the chest CT scan images so that the interpretation and the initial screening process of the COVID-19 suspected patients become easier. The proposed approach is applied to 250 CT scan images of the chest region which are collected from the COVID-19 positive patients from different geographic regions and different age groups. In this article, the results of the 10 randomly selected CT scan images are discussed and presented. Apart from these 250 CT images, 150 other images that belong to the normal category, as well as some other lung diseases, are also investigated. For the sake of conciseness, test results of only fourteen randomly selected images among these images are reported in this work. The average quantitative performance of all five algorithms (including the proposed one) is reported in Table 3 that will help to get an essence of the overall performance of the proposed method for all 400 images under consideration. Details of these fourteen CT scan images are given in Table 1 and the images along with their histograms are given in Fig. 1. It is worth mentioning here that the fourteen images for which the results are presented are collected from eight distinct patients.

The 400 images that are investigated are collected from 279 patients of different gender and various geographic locations. Among these images, 250 images are collected from 160 confirmed COVID-19 positive patients. The presence of the COVID-19 infection in the body of these patients is confirmed with the help of the RT-PCR test. In most cases, some symptoms like fever, loss of smell, headache, etc. are developed for 2–8 days. Among the rest of the 150 images, 63 images belong to the normal category and the other 87 images belong to pneumonia caused by other than COVID-19 infection.

The effect of the value of the radius on the value edge content is numerically illustrated in Table 2 and the corresponding graphical analysis is provided in Fig. 2 (please refer Eq. (5)).

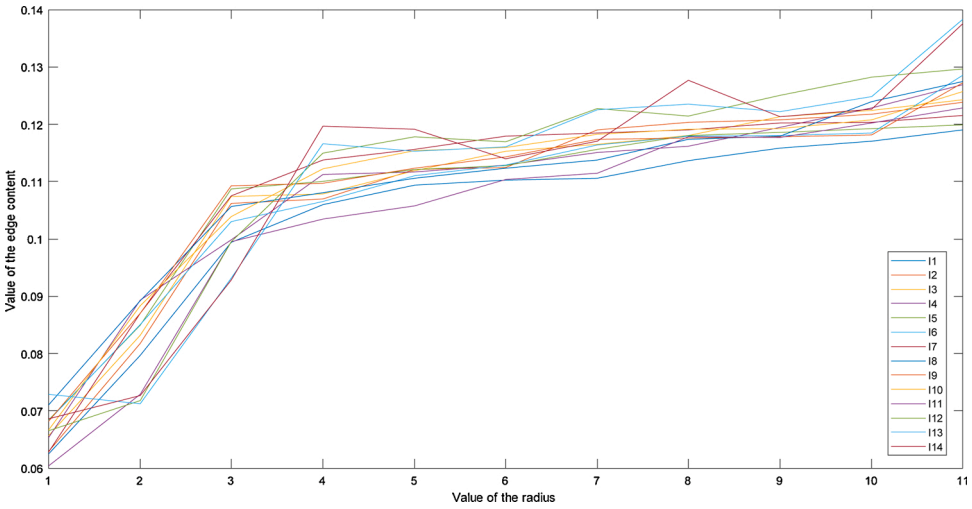

Fig. 2. Graphical analysis of the relation of the edge content on the value of the radius.

To test the performance of the proposed approach, extensive simulations are performed. The proposed approach is applied on different images to perform the segmentation operation. As discussed earlier, the prime objective of this work is to assist domain experts in easy interpretation of the CT images so that they can effectively diagnose a patient. In this section, results of the simulation and experiments are reported in detail. Experiments are performed and evaluated in both qualitative and quantitative manner.

4.1. Quantitative evaluation of the proposed approach

It may not be always possible to evaluate the results of the segmentation in a qualitative way. Therefore, it is essential to quantify the segmented outcome in some meaningful way so that some significant information can be extracted out of it. In this work, some standard quantitative evaluation metrics like peak signal to noise ratio (PSNR), mean squared error (MSE), structural similarity index (SSIM) are used assuming no ground truth segmentation data are available. These metrics are defined below.

Mean squared error and peak signal to noise ratio are two frequently used metrics that help to determine the possibility to reconstruct the actual image from the segmented outcome. These two metrics are defined in Eqs. (16) and (17) respectively.

A. Mean squared error (MSE)

The MSE is one of the frequently used statistical parameters and useful to measure the average of the squared error. It can be observed that this value can never be negative and closer to zero value indicates better performance. This parameter is often used to compare more than one statistical model. It is defined in Eq. (16).

$$MSE = \frac{1}{d_1 \times d_2} \sum_{g=1}^{d_1} \sum_{h=1}^{d_2} \left(IMG_{g,h} - IMG'_{g,h} \right) \tag{16}$$

B. Peak signal-to-noise ratio (PSNR)

Theoretically, PSNR is defined as the ratio between the maximum possible power of a signal to the power of noise. It is observed that the dynamic range of several signals is considerably wide enough and therefore, the value of the PSNR is typically presented as a logarithmic quantity (in decibel scale). The mathematical definition of PSNR is given in Eq. (17).

$$PSNR = 10\log_{10}\left(\frac{IMG_{\max}^2}{MSE} \right) \tag{17}$$

In above equations, IMG and IMG' are the actual and the segmented images respectively with size $[d_1 \times d_2]$. The maximum limit of the gray-level intensity value is denoted with $IMG_{\max}$.

C. Structural similarity index measure (SSIM)

Edges play a vital role in the structure of an image are considered as the higher frequency components and structural similarity index or SSIM gives an estimate about the higher frequency components and it is effective to quantify the segmented output. The value of SSIM can be computed using Eq. (18).

$$SSIM(IMG, IMG') = \frac{(2 \cdot \mu_{IMG} \cdot \mu_{IMG'} + \upsilon_1)(2 \cdot \sigma_{IMG,IMG'} + \upsilon_2)}{(\mu_{IMG}^2 + \mu_{IMG'}^2 + \upsilon_1)(\sigma_{IMG}^2 + \sigma_{IMG'}^2 + \upsilon_2)} \tag{18}$$

From Eq. (18), it can be observed that five different influencing parameters like mean (μ), standard deviation (σ), variance (σ^2) and two constants υ_1 and υ_2 are there. The value of mean and standard deviation can be computed using Eqs. (19) and (20) respectively.

$$\mu = \frac{\sum_{r=1}^{itrCnt} \Psi_r}{itrCnt} \tag{19}$$

$$\sigma = \frac{1}{itrCnt} \sqrt{\left(\sum_{s=1}^{itrCnt} (\Psi_s - \mu)^2 \right)} \tag{20}$$

The value of the fitness at the t^{th} iteration is represented by Ψ_t. Four standard and similar approaches from the literature are compared with the proposed approach to evaluate and establish the efficiency of the proposed method. Among these four works, the first work [62] is based on Fuzzy-C Means and morphological image processing. This work incorporates the concept of fuzzy entropy to determine the optimal threshold value. The computed threshold is adaptive and dynamic. This work is applied to CT images that are collected from Aga Khan Medical University, Pakistan. The second approach [63] is based on mathematical morphology and region merging. This approach is developed to overcome the over-segmentation problem of the watershed approach. This approach uses a multi-scale morphological approach to find the gradient image. The gradient image is helpful to remove the insignificant textures and some extremes that can be considered as noise. The watershed-based approach is used to get the initial segmented image. The region merging method is applied to obtain meaningful

Table 3
Quantitative results of the experiments (*Best values are highlighted in the bold faces*).

Image	Method	MSE	PSNR	SSIM
I^{01}	Jaffar et al. [62]	461.0236	21.49357	0.60912
	Huang et al. [63]	421.6239	21.88155	0.525154
	Jaffar et al. [65]	371.0915	22.43599	0.717395
	Kim et al. [64]	430.3605	21.79248	0.475448
	Proposed	**386.5459**	**22.25879**	**0.869885**
I^{02}	Jaffar et al. [62]	362.4469	22.53836	0.76712
	Huang et al. [63]	386.3293	22.26123	0.83904
	Jaffar et al. [65]	418.2887	21.91604	0.306594
	Kim et al. [64]	402.4168	22.08404	0.835875
	Proposed	**309.365**	**23.2260918**	**0.960307**
I^{03}	Jaffar et al. [62]	436.7762	21.72821	0.259875
	Huang et al. [63]	413.0066	21.97123	0.775217
	Jaffar et al. [65]	399.0454	22.12058	0.714363
	Kim et al. [64]	390.5551	22.21398	0.583544
	Proposed	**389.2042**	**22.22903**	**0.898072**
I^{04}	Jaffar et al. [62]	370.2903	22.44538	0.637983
	Huang et al. [63]	418.4449	21.91442	0.482619
	Jaffar et al. [65]	390.6476	22.21295	0.376222
	Kim et al. [64]	414.9244	21.95111	0.465437
	Proposed	**345.2344**	**22.749662**	**0.836166**
I^{05}	Jaffar et al. [62]	442.0584	21.67601	**0.925052**
	Huang et al. [63]	391.8134	22.20001	0.843646
	Jaffar et al. [65]	383.1398	22.29723	0.112416
	Kim et al. [64]	428.4173	21.81213	0.639128
	Proposed	**335.9571**	**22.86796**	0.792513
I^{06}	Jaffar et al. [62]	372.7697	22.4164	0.967129
	Huang et al. [63]	398.5772	22.12568	0.56672
	Jaffar et al. [65]	462.6236	21.47853	0.51015
	Kim et al. [64]	455.5487	21.54546	**0.96785**
	Proposed	**321.2911**	**23.06181**	0.951481
I^{07}	Jaffar et al. [62]	435.5595	21.74033	0.63594
	Huang et al. [63]	405.6508	22.04928	0.341634
	Jaffar et al. [65]	**373.2901**	**22.41034**	0.673696
	Kim et al. [64]	416.5986	21.93363	0.772775
	Proposed	398.5379	22.12611	**0.96839**
I^{08}	Jaffar et al. [62]	450.8064	21.5909	0.846886
	Huang et al. [63]	**370.4987**	**22.44294**	0.594791
	Jaffar et al. [65]	379.9465	22.33358	0.44244
	Kim et al. [64]	380.6872	22.32512	0.343784
	Proposed	377.8177	22.35798	**0.969866**
I^{09}	Jaffar et al. [62]	459.4273	21.50864	0.200482
	Huang et al. [63]	412.7194	21.97425	0.670061
	Jaffar et al. [65]	411.8386	21.98353	0.465865
	Kim et al. [64]	453.304	21.56691	0.433878
	Proposed	**367.0179**	**22.48393**	**0.949287**
I^{10}	Jaffar et al. [62]	445.8447	21.63897	0.661575
	Huang et al. [63]	369.961	22.44924	0.876597
	Jaffar et al. [65]	450.8862	21.59013	**0.91903**
	Kim et al. [64]	393.7542	22.17855	0.77023
	Proposed	**311.0236**	**23.20287**	0.80912
I^{11}	Jaffar et al. [62]	446.3279	21.23367	0.758761
	Huang et al. [63]	389.7223	23.01971	0.82457
	Jaffar et al. [65]	460.7305	21.56451	0.838475
	Kim et al. [64]	399.2441	21.53991	0.984545
	Proposed	**317.562**	**23.13616**	**0.99592**
I^{12}	Jaffar et al. [62]	444.9836	21.08579	0.7259
	Huang et al. [63]	370.2262	22.48187	0.866943
	Jaffar et al. [65]	401.1307	21.33911	0.865812
	Kim et al. [64]	343.2678	22.16337	**0.969596**
	Proposed	**321.6708**	**22.96078**	0.952138
I^{13}	Jaffar et al. [62]	447.2416	21.21015	**0.953423**
	Huang et al. [63]	378.6596	22.8543	0.951248
	Jaffar et al. [65]	403.7622	21.93808	0.746991
	Kim et al. [64]	348.1695	20.66917	0.850249
	Proposed	**323.8248**	**23.30248**	0.950369
I^{14}	Jaffar et al. [62]	440.2179	19.97012	0.855519
	Huang et al. [63]	378.5488	21.6787	0.726767
	Jaffar et al. [65]	396.1929	19.6233	0.830601
	Kim et al. [64]	343.2488	22.28335	0.946276
	Proposed	**328.7019**	**23.72202**	**0.974978**
Overall Average (400 images)	Jaffar et al. [62]	409.4028521	21.6239624	0.744735144
	Huang et al. [63]	379.5005211	21.109975	0.774113815
	Jaffar et al. [65]	447.7915437	21.3701288	0.714503014
	Kim et al. [64]	382.9325718	22.6863406	0.829478584
	Proposed	**307.1888625**	**23.7246505**	**0.831718459**

segmentation. The third approach [54] proposes a method for lung CT image segmentation that is based on morphological image processing and genetic algorithm. The genetic algorithm is used to compute the threshold values. This approach is a fully automated system that can be deployed to segment lung CT images. The fourth approach [64] designed to perform lung CT image segmentation is based on anisotropic diffusion and morphological operation. This work comprises three stages. This work begins by converting a gray image that is converted into a blurred one with the help of anisotropic diffusion. In the second

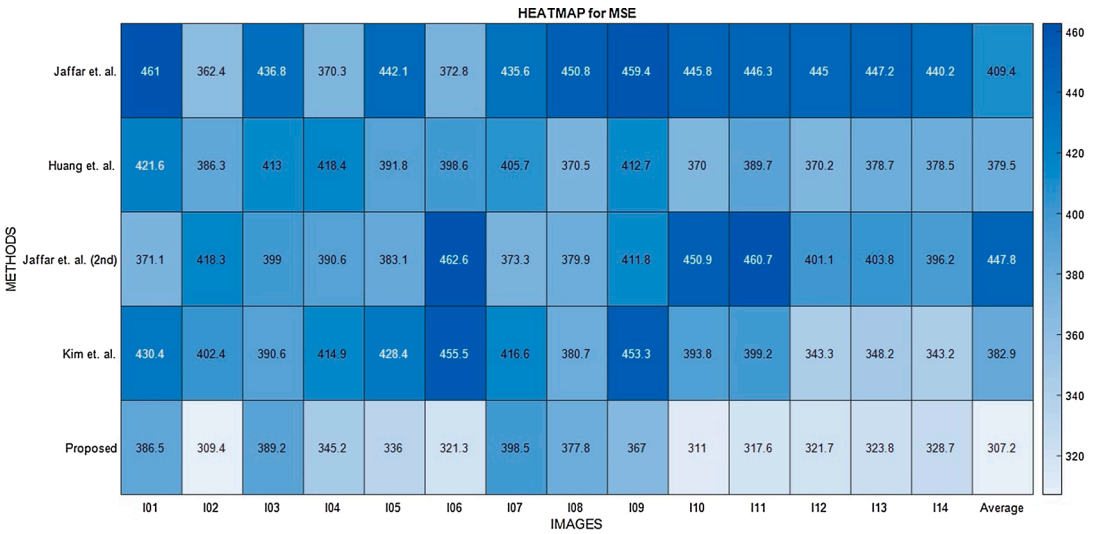

(a)

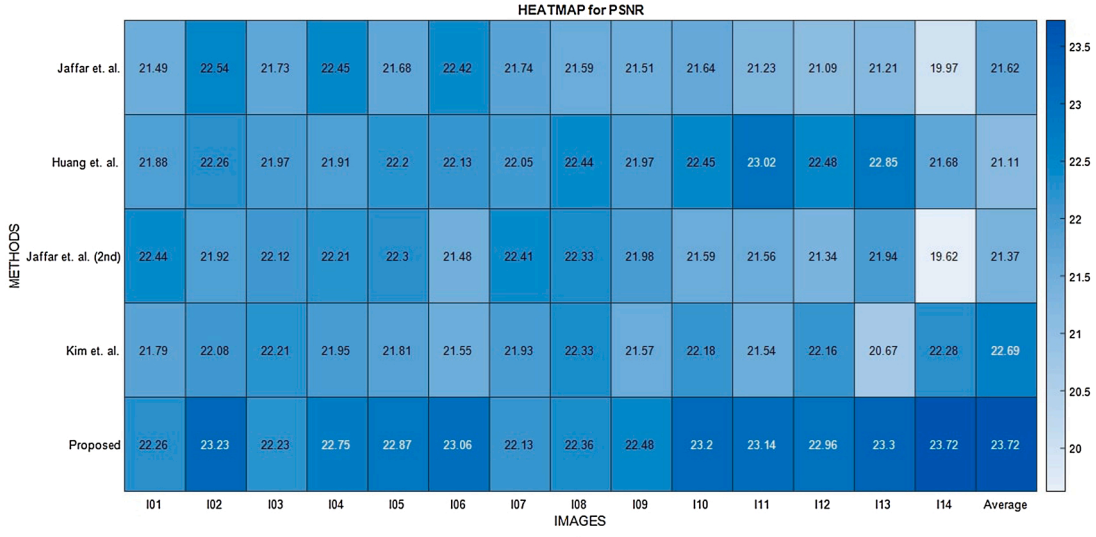

(b)

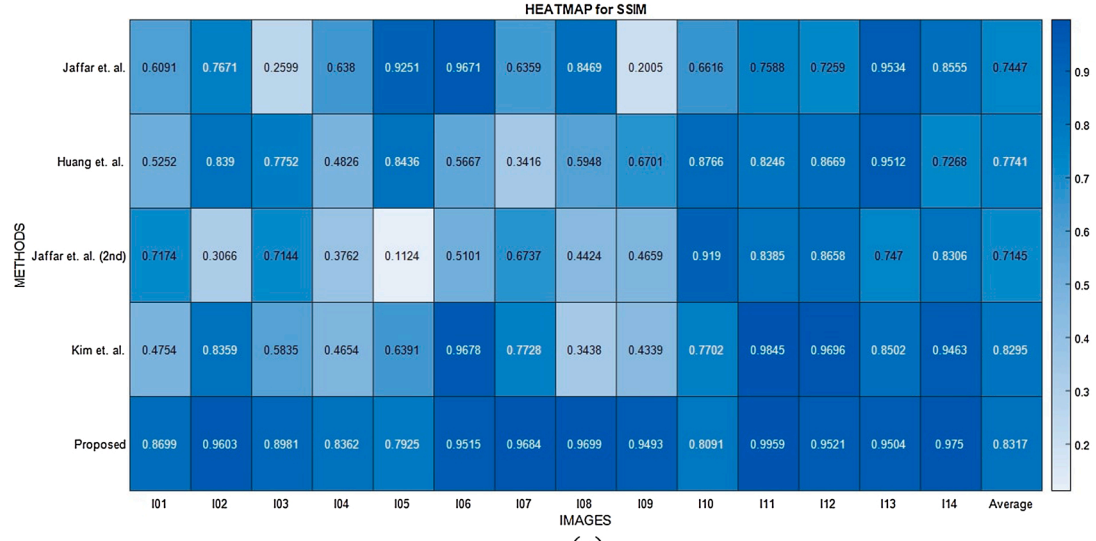

(c)

Fig. 3. Heatmap of (a) MSE, (b) PSNR, and (c) SSIM.

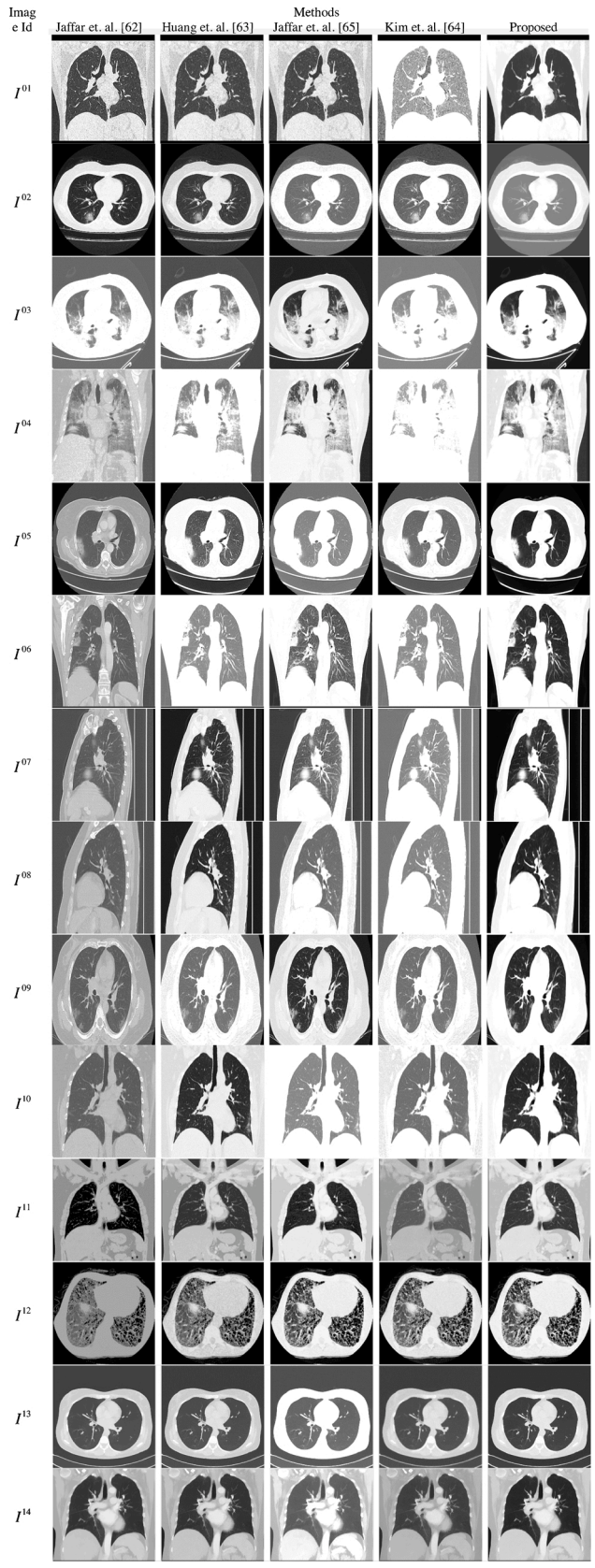

Fig. 4. Segmented outputs of fourteen images using different approaches.

step, the airway and mediastinum are removed with the help of morphological operations. In the third step, a binary image of the left and right lung is obtained that is matched with the original image to obtain the segmented outcome. Table 3 reports the obtained quantitative results along with a comparative overview and corresponding heatmaps are provided in Fig. 3. Three heatmaps are provided for three validation parameters. In the x-axis, the images are plotted and, in the y-axis, five different methods are plotted.

4.2. Qualitative evaluation of the proposed approach

The performance of the proposed approach is evaluated and compared with some other standard existing approaches qualitatively. In this subsection, the results of the qualitative evaluation are presented in detail. Fig. 4 shows the segmented outcome after applying five different approaches.

The overall average values of 400 images are reported in Table 3 that proves that the proposed approach is efficient enough in segmenting different CT images and effectively provides better performance compared to some state-of-the-art approaches. It can be observed that, on average, the proposed approach achieves minimum MSE, maximum PSNR, and SSIM values compared to the other four standard approaches that prove the superiority of the proposed approach. Moreover, experiments are carried out on various healthy images and the experimental outcomes prove that the proposed approach can simultaneously perform well for both COVID-19 infected chest CT images and normal chest CT images. The segmented outcomes show that the proposed approach can effectively perform the job of segmentation without the help of any manual delineations.

Although the quantitative results are quite promising and show the effectiveness of the proposed approach still, the qualitative results must be investigated properly. It is always better to compare any segmentation approach with some manual delineations so that, an idea of the qualitative performance can be obtained. But manual delineations are hard to obtain because it involves domain experts. It is a difficult and time-consuming task and therefore, the manual delineations that can serve as the ground truth segmentation are difficult to obtain for the COVID-19 image dataset. But the obtained segmented outcomes can be visually investigated to get an essence of the performance. It can be observed that the proposed approach can effectively segment different regions of the CT images under consideration. From the detailed qualitative and quantitative analysis, it can be easily observed that the proposed approach outperforms most of the standard approaches. The segmented outputs which are obtained after applying the proposed approach are quite better compared to other approaches which are certainly helpful for the physicians to assess the suspected patients in a non-invasive manner. This approach is also helpful to perform massive testing with realistic segmented outputs which is beneficial to stop the drastic spread of the COVID-19 disease. A specific approach may act differently for different types of images. From Fig. 1 it can be observed that the same method (e.g., Jaffar et al. [62]) is behaving in a different manner for two similar kinds of images I^{01} and I^{04}. It is to be noted that the histogram of the image I^{01} and I^{04} are different and histogram or the pixel intensity distribution is one of the key factors that directly affect the performance of a segmentation approach.

The proposed approach is designed to assist the domain experts and physicians in easy interpretation of the radiological images. This work never claims that the proposed approach can replace the standard tests like RT-PCR that is the gold standard to detect the presence of COVID-19. Radiologists, physicians, and other domain experts are highly capable to interpret radiological images. Moreover, in most cases, human experts can interpret a radiological image very quickly compared to computer-aided systems. However, most of the human experts work under tremendous pressure specifically under any pandemic scenario like this. This approach is dedicated to reducing the inherent human

errors to some extent by performing efficient segmentation before manual investigations. The proposed approach cannot eliminate the involvement of human experts because this approach is not designed to diagnose radiological images and automatically take decisions. This approach is designed to make the job the human experts simpler.

5. Conclusion

The main objective of the proposed approach is to propose a computer-aided solution that can assist the physicians and other domain experts in early screening and assessment of the COVID-19 suspected patients by analyzing the radiological images. It is also helpful to maintain an appropriate distance from the suspected person that ensures the safety of the health workers. The proposed approach helps to automatically identify different regions of the CT image which is helpful to interpret different signs of the COVID-19 infection from the chest CT scan images. The efficiency of the proposed approach was established by applying the proposed method on various real-life CT scan images that are collected from the COVID-19 infected patients. Both quantitative and qualitative analysis of the proposed approach proves the efficiency and the real-life applicability of this approach. Moreover, the comparative study shows that the proposed approach is efficient enough to outperform some of the existing in the concerned domain. So, the proposed approach addresses a challenging problem with strong real-life utility. In future works, the proposed approach can be enhanced in various ways. For example, the elliptic shape fitting approach can be automated in such a way so that, the penalty terms can be minimized. Moreover, the duty to find the range of the infected area can be transferred to the shoulder of the automated and intelligent processes. Some interesting features can be mined from these images which may help to further enhance this proposed approach. But the proposed approach can be really helpful in the mid of this pandemic scenario and can assist the physicians and other domain experts in the easy and quick interpretation of the radiological images. The proposed approach can also be applied to detect some other diseases from different modalities of the biomedical images.

CRediT authorship contribution statement

Prof. Kalyani Mali supported and has significant contribution in formal analysis, resources, review, editing, and supervision. **Mr. Shouvik Chakraborty** has a major contribution in solution formulation, conceptualization, Methodology, Software development, article writing, and investigation.

Declaration of Competing Interest

The authors declare that they have no known competing financial interests or personal relationships that could have appeared to influence the work reported in this paper.

References

[1] WHO Coronavirus (COVID-19) Dashboard, WHO Coronavirus (COVID-19) Dashboard With Vaccination Data, 2021 (n.d.). https://covid19.who.int/ (Accessed 20 April 2021).

[2] E.A. Akl, I. Blazic, S. Yaacoub, G. Frija, R. Chou, J.A. Appiah, M. Fatehi, N. Flor, E. Hitti, H. Jafri, Z.Y. Jin, H.U. Kauczor, M. Kawooya, E.A. Kazerooni, J.P. Ko, R. Mahfouz, V. Muglia, R. Nyabanda, M. Sanchez, P.B. Shete, M. Ulla, C. Zheng, E. Van Deventer, M. Del Rosario Perez, Use of chest imaging in the diagnosis and management of COVID-19: a WHO rapid advice guide, Radiology 298 (2021) E63–E69, https://doi.org/10.1148/RADIOL.2020203173.

[3] A. Axiaq, A. Almohtadi, S.A. Massias, D. Ngemoh, A. Harky, The role of computed tomography scan in the diagnosis of COVID-19 pneumonia, Curr. Opin. Pulm. Med. 27 (2021) 163–168, https://doi.org/10.1097/MCP.0000000000000765.

[4] M. Mossa-Basha, C.C. Meltzer, D.C. Kim, M.J. Tuite, K.P. Kolli, B.S. Tan, Radiology department preparedness for COVID-19: radiology scientific expert review panel, Radiology 296 (2020) E106–E112, https://doi.org/10.1148/radiol.2020200988.

[5] A. Kumar, P.K. Gupta, A. Srivastava, A review of modern technologies for tackling COVID-19 pandemic, Diabetes Metab. Syndr. Clin. Res. Rev. 14 (2020) 569–573, https://doi.org/10.1016/j.dsx.2020.05.008.

[6] F. Shi, J. Wang, J. Shi, Z. Wu, Q. Wang, Z. Tang, K. He, Y. Shi, D. Shen, Review of artificial intelligence techniques in imaging data acquisition, segmentation and diagnosis for COVID-19, IEEE Rev. Biomed. Eng. (2020), https://doi.org/10.1109/RBME.2020.2987975.

[7] D.L. Smith, J.-P. Grenier, C. Batte, B. Spieler, A characteristic chest radiographic pattern in the setting of the COVID-19 pandemic, Radiol. Cardiothorac. Imaging 2 (2020), e200280, https://doi.org/10.1148/ryct.2020200280.

[8] M.U. Nasir, J. Roberts, N.L. Muller, F. Macri, M.F. Mohammed, S. Akhlaghpoor, W. Parker, A. Eftekhari, S. Rezaei, J. Mayo, S. Nicolaou, The role of emergency radiology in COVID-19: from preparedness to diagnosis, Can. Assoc. Radiol. J. 71 (2020) 293–300, https://doi.org/10.1177/0846537120916419.

[9] P. López-Úbeda, M.C. Díaz-Galiano, T. Martín-Noguerol, A. Luna, L.A. Ureña-López, M.T. Martín-Valdivia, COVID-19 detection in radiological text reports integrating entity recognition, Comput. Biol. Med. 127 (2020), 104066, https://doi.org/10.1016/j.compbiomed.2020.104066.

[10] S. Chakraborty, K. Mali, SUFMACS: a machine learning-based robust image segmentation framework for covid-19 radiological image interpretation, Expert Syst. Appl. (2021), 115069, https://doi.org/10.1016/j.eswa.2021.115069.

[11] J.P. Kanne, B.P. Little, J.H. Chung, B.M. Elicker, L.H. Ketai, Essentials for radiologists on COVID-19: an update-radiology scientific expert panel, Radiology (2020), 200527, https://doi.org/10.1148/radiol.2020200527.

[12] Y. Fang, H. Zhang, J. Xie, M. Lin, L. Ying, P. Pang, W. Ji, Sensitivity of chest CT for COVID-19: comparison to RT-PCR, Radiology (2020), 200432, https://doi.org/10.1148/radiol.2020200432.

[13] A. Bernheim, X. Mei, M. Huang, Y. Yang, Z.A. Fayad, N. Zhang, K. Diao, B. Lin, X. Zhu, K. Li, S. Li, H. Shan, A. Jacobi, M. Chung, Chest CT findings in coronavirus disease-19 (COVID-19): relationship to duration of infection, Radiology (2020), 200463, https://doi.org/10.1148/radiol.2020200463.

[14] T. Ai, Z. Yang, H. Hou, C. Zhan, C. Chen, W. Lv, Q. Tao, Z. Sun, L. Xia, Correlation of chest CT and RT-PCR testing in coronavirus disease 2019 (COVID-19) in China: a report of 1014 cases, Radiology (2020), 200642, https://doi.org/10.1148/radiol.2020200642.

[15] S. Chakraborty, S. Chatterjee, N. Dey, A.S. Ashour, A.S. Ashour, F. Shi, K. Mali, Modified cuckoo search algorithm in microscopic image segmentation of hippocampus, Microsc. Res. Tech. 80 (2017) 1051–1072, https://doi.org/10.1002/jemt.22900.

[16] S. Hore, S. Chakroborty, A.S. Ashour, N. Dey, A.S. Ashour, D. Sifaki-Pistolla, T. Bhattacharya, S.R.B. Chaudhuri, Finding contours of hippocampus brain cell using microscopic image analysis, J. Adv. Microsc. Res. 10 (2015) 93–103, https://doi.org/10.1166/jamr.2015.1245.

[17] S. Hore, S. Chakraborty, S. Chatterjee, N. Dey, A.S. Ashour, L. Van Chung, D.-N. Le, An integrated interactive technique for image segmentation using stack based seeded region growing and thresholding, Int. J. Electr. Comput. Eng. 6 (2016), https://doi.org/10.11591/ijece.v6i6.11801.

[18] H. Cui, H. Wang, K. Yan, X. Wang, W. Zuo, D.D. Feng, Biomedical image segmentation for precision radiation oncology. Biomed. Inf. Technol., Elsevier, 2020, pp. 295–319, https://doi.org/10.1016/B978-0-12-816034-3.00010-9.

[19] S. Chakraborty, An advanced approach to detect edges of digital images for image segmentation, in: S. Chakraborty, K. Mali (Eds.), Appl. Adv. Mach. Intell. Comput. Vis. Object Recognit. Emerg. Res. Oppor., IGI GLobal, 2020, https://doi.org/10.4018/978-1-7998-2736-8.ch004.

[20] S. Chakraborty, K. Mali, An overview of biomedical image analysis from the deep learning perspective, in: S. Chakraborty, K. Mali (Eds.), Appl. Adv. Mach. Intell. Comput. Vis. Object Recognit. Emerg. Res. Oppor., IGI Global, 2020, https://doi.org/10.4018/978-1-7998-2736-8.ch008.

[21] S. Chakraborty, K. Mali, Application of multiobjective optimization techniques in biomedical image segmentation—a study. Multi-Objective Optim., Springer, Singapore, Singapore, 2018, pp. 181–194, https://doi.org/10.1007/978-981-13-1471-1_8.

[22] S. Chakraborty, K. Mali, Fuzzy Electromagnetism Optimization (FEMO) and its application in biomedical image segmentation, Appl. Soft Comput. 97 (2020), 106800, https://doi.org/10.1016/j.asoc.2020.106800.

[23] N. Papernot, M. Abadi, Ú. Erlingsson, I. Goodfellow, K. Talwar, Semi-Supervised Knowledge Transfer for Deep Learning from Private Training Data, 2016. http://arxiv.org/abs/1610.05755.

[24] S. Chakraborty, K. Mali, A. Banerjee, M. Bhattacharjee, A Biomedical Image Segmentation Approach Using Fractional Order Darwinian Particle Swarm Optimization and Thresholding, Springer, Singapore, 2021, pp. 299–306, https://doi.org/10.1007/978-981-15-9433-5_29.

[25] A. Tchagna Kouanou, D. Tchiotsop, R. Kengne, D.T. Zephirin, N.M. Adele Armele, R. Tchinda, An optimal big data workflow for biomedical image analysis, Informatics Med. Unlocked 11 (2018) 68–74, https://doi.org/10.1016/j.imu.2018.05.001.

[26] S. Chakraborty, K. Mali, A. Banerjee, M. Bhattacharjee, S. Chatterjee, Image segmentation based on galactic swarm optimization. Lect. Notes Networks Syst., Springer Science and Business Media Deutschland GmbH, 2021, pp. 251–258, https://doi.org/10.1007/978-981-15-9433-5_24.

[27] S. Chakraborty, S. Bhowmik, Blending roulette wheel selection with simulated annealing for job shop scheduling problem, in: Michael Faraday IET Int. Summit 2015, Institution of Engineering and Technology, 2015, https://doi.org/10.1049/cp.2015.1696, pp. 100 (7.)-100 (7.).

[28] S. Chakraborty, S. Chatterjee, A.S. Ashour, K. Mali, N. Dey, Intelligent computing in medical imaging: a study, in: N. Dey (Ed.), Adv. Appl. Metaheuristic Comput.,

IGI Global, 2017, pp. 143–163, https://doi.org/10.4018/978-1-5225-4151-6.ch006.
[29] S. Chakraborty, K. Mali, SuFMoFPA: a superpixel and meta-heuristic based fuzzy image segmentation approach to explicate COVID-19 radiological images, Expert Syst. Appl. (2020), 114142, https://doi.org/10.1016/j.eswa.2020.114142.
[30] E.E.-D. Hemdan, M.A. Shouman, M.E. Karar, COVIDX-Net: a Framework of Deep Learning Classifiers to Diagnose COVID-19 in X-Ray Images, 2020. http://arxiv.org/abs/2003.11055.
[31] L. Wang, A. Wong, COVID-Net: A Tailored Deep Convolutional Neural Network Design for Detection of COVID-19 Cases from Chest X-Ray Images, 2020. http://arxiv.org/abs/2003.09871.
[32] T. Ozturk, M. Talo, E.A. Yildirim, U.B. Baloglu, O. Yildirim, U. Rajendra Acharya, Automated detection of COVID-19 cases using deep neural networks with X-ray images, Comput. Biol. Med. 121 (2020), 103792, https://doi.org/10.1016/j.compbiomed.2020.103792.
[33] F. Ucar, D. Korkmaz, COVIDiagnosis-Net: deep Bayes-SqueezeNet based diagnosis of the coronavirus disease 2019 (COVID-19) from X-ray images, Med. Hypotheses 140 (2020), 109761, https://doi.org/10.1016/j.mehy.2020.109761.
[34] I.D. Apostolopoulos, T.A. Mpesiana, Covid-19: automatic detection from X-ray images utilizing transfer learning with convolutional neural networks, Phys. Eng. Sci. Med. 43 (2020) 635–640, https://doi.org/10.1007/s13246-020-00865-4.
[35] X. Chen, Y. Tang, Y. Mo, S. Li, D. Lin, Z. Yang, Z. Yang, H. Sun, J. Qiu, Y. Liao, J. Xiao, X. Chen, X. Wu, R. Wu, Z. Dai, A diagnostic model for coronavirus disease 2019 (COVID-19) based on radiological semantic and clinical features: a multi-center study, Eur. Radiol. (2020), https://doi.org/10.1007/s00330-020-06829-2 (n.d.).
[36] O. Gozes, M. Frid-Adar, H. Greenspan, P.D. Browning, H. Zhang, W. Ji, A. Bernheim, E. Siegel, Rapid AI Development Cycle for the Coronavirus (COVID-19) Pandemic: Initial Results for Automated Detection & Patient Monitoring Using Deep Learning CT Image Analysis, 2020. http://arxiv.org/abs/2003.05037.
[37] L. Huang, R. Han, T. Ai, P. Yu, H. Kang, Q. Tao, L. Xia, Serial quantitative chest CT assessment of COVID-19: deep-learning approach, Radiol. Cardiothorac. Imaging 2 (2020), e200075, https://doi.org/10.1148/ryct.2020200075.
[38] D. Singh, V. Kumar, Vaishali, M. Kaur, Classification of COVID-19 patients from chest CT images using multi-objective differential evolution-based convolutional neural networks, Eur. J. Clin. Microbiol. Infect. Dis. (2020), https://doi.org/10.1007/s10096-020-03901-z/Published (n.d.).
[39] Q. Yao, L. Xiao, P. Liu, S.K. Zhou, Label-Free Segmentation of COVID-19 Lesions in Lung CT, 2020 http://arxiv.org/abs/2009.06456 (Accessed 4 October 2020).
[40] A. Mohammed, C. Wang, M. Zhao, M. Ullah, R. Naseem, H. Wang, M. Pedersen, F. A. Cheikh, Weakly-supervised network for detection of COVID-19 in chest CT scans, IEEE Access 8 (2020) 155987–156000, https://doi.org/10.1109/ACCESS.2020.3018498.
[41] J. Ma, Z. Nie, C. Wang, G. Dong, Q. Zhu, J. He, L. Gui, X. Yang, Active contour regularized semi-supervised learning for COVID-19 CT infection segmentation with limited annotations, Phys. Med. Biol. 65 (2020), 225034, https://doi.org/10.1088/1361-6560/abc04e.
[42] T. Zheng, M. Oda, C. Wang, T. Moriya, Y. Hayashi, Y. Otake, M. Hashimoto, T. Akashi, M. Mori, H. Takabatake, H. Natori, K. Mori, Unsupervised segmentation of COVID-19 infected lung clinical CT volumes using image inpainting and representation learning, in: B.A. Landman, I. Išgum (Eds.), Med. Imaging 2021 Image Process, SPIE, 2021, p. 120, https://doi.org/10.1117/12.2580641.
[43] R. Vaishya, M. Javaid, I.H. Khan, A. Haleem, Artificial Intelligence (AI) applications for COVID-19 pandemic, Diabetes Metab. Syndr. Clin. Res. Rev. 14 (2020) 337–339, https://doi.org/10.1016/j.dsx.2020.04.012.
[44] R. Bhayana, A. Som, M.D. Li, D.E. Carey, M.A. Anderson, M.A. Blake, O. Catalano, M.S. Gee, P.F. Hahn, M. Harisinghani, A. Kilcoyne, S.I. Lee, A. Mojtahed, P. V. Pandharipande, T.T. Pierce, D.A. Rosman, S. Saini, A.E. Samir, J.F. Simeone, D. A. Gervais, G. Velmahos, J. Misdraji, A. Kambadakone, Abdominal imaging findings in COVID-19: preliminary observations, Radiology (2020), 201908, https://doi.org/10.1148/radiol.2020201908.
[45] M.E.H. Chowdhury, T. Rahman, A. Khandakar, R. Mazhar, M.A. Kadir, Z. Bin Mahbub, K.R. Islam, M.S. Khan, A. Iqbal, N. Al-Emadi, M.B.I. Reaz, T.I. Islam, Can AI Help in Screening Viral and COVID-19 Pneumonia?, 2020. http://arxiv.org/abs/2003.13145.
[46] A. Ulhaq, A. Khan, D. Gomes, M. Paul, Computer Vision for COVID-19 Control: a Survey, 2020. http://arxiv.org/abs/2004.09420.
[47] R.C. Gonzalez, Richard E. Woods, Digital Image Processing, Prentice Hall, 2008.
[48] A. Saleem, A. Beghdadi, B. Boashash, Image fusion-based contrast enhancement, EURASIP J. Image Video Process. 2012 (2012) 10, https://doi.org/10.1186/1687-5281-2012-10.
[49] X.H. Yao, T.Y. Li, Z.C. He, Y.F. Ping, H.W. Liu, S.C. Yu, H.M. Mou, L.H. Wang, H. R. Zhang, W.J. Fu, T. Luo, F. Liu, C. Chen, H.L. Xiao, H.T. Guo, S. Lin, D.F. Xiang, Y. Shi, Q.R. Li, X. Huang, Y. Cui, X.Z. Li, W. Tang, P.F. Pan, X.Q. Huang, Y.Q. Ding, X.W. Bian, A pathological report of three COVID-19 cases by minimally invasive autopsies, Zhonghua Bing Li Xue Za Zhi = Chin. J. Pathol. 49 (2020) E009, https://doi.org/10.3760/cma.j.cn112151-20200312-00193.
[50] D. McGonagle, J.S. O'Donnell, K. Sharif, P. Emery, C. Bridgewood, Immune mechanisms of pulmonary intravascular coagulopathy in COVID-19 pneumonia, Lancet Rheumatol. 2 (2020) e437–e445, https://doi.org/10.1016/S2665-9913(20)30121-1.
[51] J.B. Forrest, The effect of changes in lung volume on the size and shape of alveoli, J. Physiol. 210 (1970) 533–547, https://doi.org/10.1113/jphysiol.1970.sp009225.
[52] M. Ochs, J.R. Nyengaard, A. Jung, L. Knudsen, M. Voigt, T. Wahlers, J. Richter, H. J.G. Gundersen, The number of alveoli in the human lung, Am. J. Respir. Crit. Care Med. 169 (2004) 120–124, https://doi.org/10.1164/rccm.200308-1107oc.
[53] A. Fitzgibbon, M. Pilu, R.B. Fisher, Direct least square fitting of ellipses, IEEE Trans. Pattern Anal. Mach. Intell. 21 (1999) 476–480, https://doi.org/10.1109/34.765658.
[54] COVID-19 pneumonia | Radiology Case | Radiopaedia.org, (n.d.). https://radiopaedia.org/cases/covid-19-pneumonia-29 (Accessed 6 May 2020).
[55] COVID-19 pneumonia | Radiology Case | Radiopaedia.org, (n.d.). https://radiopaedia.org/cases/covid-19-pneumonia-12 (Accessed 10 June 2020).
[56] COVID-19 pneumonia | Radiology Case | Radiopaedia.org, (n.d.). https://radiopaedia.org/cases/covid-19-pneumonia-63 (Accessed 31 May 2020).
[57] COVID-19 pneumonia | Radiology Case | Radiopaedia.org, (n.d.). https://radiopaedia.org/cases/covid-19-pneumonia-88 (Accessed 10 June 2020).
[58] Normal CT chest | Radiology Case | Radiopaedia.org, (n.d.). https://radiopaedia.org/cases/normal-ct-chest (Accessed 5 March 2021).
[59] Usual interstitial pneumonia (UIP) | Radiology Case | Radiopaedia.org, (n.d.). https://radiopaedia.org/cases/usual-interstitial-pneumonia-uip?lang=us (Accessed 5 March 2021).
[60] Normal chest CT | Radiology Case | Radiopaedia.org, (n.d.). https://radiopaedia.org/cases/normal-chest-ct-1?lang=gb (Accessed 8 May 2021).
[61] Pulmonary mucormycosis | Radiology Case | Radiopaedia.org, (n.d.). https://radiopaedia.org/cases/pulmonary-mucormycosis-1?lang=gb (Accessed 8 May 2021).
[62] M. Arfan Jaffar, A. Hussain, A.M. Mirza, A. Chaudhry, Fuzzy Entropy and Morphology Based Fully Automated Segmentation of Lungs from C.T. Scan Images, 2009.
[63] H. Zhan-peng, Y. Fa-ling, Z. Su-juan, B. Su-su, Medical CT image segmentation based on mathematical morphology and region merging, Appl. Res. Comput. (2010) http://en.cnki.com.cn/Article_en/CJFDTotal-JSYJ201011103.htm (Accessed 31 July 2020).
[64] H.S. Kim, H. Yoon, K.N. Trung, G.S. Lee, Automatic Lung Segmentation in CT Images Using Anisotropic Diffusion and Morphology Operation, Institute of Electrical and Electronics Engineers (IEEE), 2008, pp. 557–561, https://doi.org/10.1109/cit.2007.143.
[65] M.A. Jaffar, A. Hussain, M. Nazir, A.M. Mirza, A. Chaudhry, GA and morphology based automated segmentation of lungs from CT scan images, in: 2008 Int. Conf. Comput. Intell. Model. Control Autom., CIMCA 2008, 2008, pp. 265–270, https://doi.org/10.1109/CIMCA.2008.168.